INTERNATIONAL JOURNAL FOR NUMERICAL METHODS IN FLUIDS
Int. J. Numer. Meth. Fluids 2007; **53**:1847–1862
Published online 2 November 2006 in Wiley InterScience (www.interscience.wiley.com). DOI: 10.1002/fld.1385

Numerical simulation of fully nonlinear irregular wave tank in three dimension

D. Z. Ning and B. Teng*, †

State Key Laboratory of Coastal and Offshore Engineering, Dalian University of Technology, Dalian 116023, China

SUMMARY

A fully nonlinear irregular wave tank has been developed using a three-dimensional higher-order boundary element method (HOBEM) in the time domain. The Laplace equation is solved at each time step by an integral equation method. Based on image theory, a new Green function is applied in the whole fluid domain so that only the incident surface and free surface are discretized for the integral equation. The fully nonlinear free surface boundary conditions are integrated with time to update the wave profile and boundary values on it by a semi-mixed Eulerian–Lagrangian time marching scheme. The incident waves are generated by feeding analytic forms on the input boundary and a ramp function is introduced at the start of simulation to avoid the initial transient disturbance. The outgoing waves are sufficiently dissipated by using a spatially varying artificial damping on the free surface before they reach the downstream boundary. Numerous numerical simulations of linear and nonlinear waves are performed and the simulated results are compared with the theoretical input waves. Copyright © 2006 John Wiley & Sons, Ltd.

Received 14 February 2006; Revised 1 September 2006; Accepted 6 September 2006

KEY WORDS: fully nonlinearity; irregular waves; numerical wave tank; higher-order boundary element method

1. INTRODUCTION

Ocean waves are generally recognized to have properties of not single frequency regularity but irregularity composed of multi-frequency components. And the wave conditions encountered for

*Correspondence to: B. Teng, State Key Laboratory of Coastal and Offshore Engineering, Dalian University of Technology, Dalian 116023, China.
†E-mail: bteng@dlut.edu.cn

Contract/grant sponsor: Program for Changjiang Scholars and Innovative Research Team in University; contract/grant number: IRT0420
Contract/grant sponsor: Research Fund for the Doctoral Program of Higher Education; contract/grant number: 20030141006

ocean or coastal structural design often exceed the validity range of small amplitude wave theory. Therefore, prediction of fully nonlinear irregular wave propagation and wave loads in the time domain is a much more important topic.

During the past few years, due to the continuous and substantial increase in computer power, numerous numerical methods have been proposed to account for the effect of wave nonlinearity. However, most researches have been conducted on the nonlinear regular waves. For instance, Xu [1], Romate [2], Kim and Kim [3] employed the higher-order boundary element method (HOBEM) to simulate fully nonlinear waves; Celebi [4], Scorpio *et al.* [5] and Beck [6] adopted the desingularized boundary integral equation method to calculate fully nonlinear wave loads on objects; Wu *et al.* [7], Hu [8], Wang and Khoo [9] used the finite element method to study the fully nonlinear water wave problems. Literatures for the simulation of the irregular waves are relatively limited, such as Xu *et al.* [10] and Boo [11]. Simulation of fully nonlinear irregular waves in the time domain requires a robust numerical scheme because of numerical instability, expensive computational cost and large computer storage [12].

In this paper, an efficient three-dimensional HOBEM is developed to simulate the fully nonlinear irregular numerical wave tank in the time domain. The boundary integral equation is formulated with quadratic-order elements and repeatedly solved at each time step. A new Green function is used based on image theory; therefore the discretized elements are only distributed on the incident surface and free surface. Theoretical waves are given as the incident waves and gradually increase from zero to the actual value for reduction of the transient disturbance. At the downtank, an artificial absorbing damping layer is employed on the free surface. The instantaneous free surface is updated at each time step by the fourth order Runge–Kutta time integration scheme. The input waves used in the present work are linear regular and irregular waves for the linear wave simulation, and the second-order regular and irregular Stokes waves for the nonlinear wave simulation. The second-order irregular waves are generated from the combination of two or four wave components. Numerous calculations are carried out and the numerical results show that the proposed scheme has a high accuracy and good numerical stability.

2. MATHEMATICAL FORMULATION

2.1. Boundary value problem

The origin of the Cartesian coordinate system is in the plane of the undisturbed free surface with the x-axis positive in the direction of incoming wave propagation and the z-axis positive in the opposite direction of gravity, as shown in Figure 1.

It is assumed that the fluid is incompressible, inviscid, and the flow irrotational. Therefore, a velocity potential $\phi(x, y, z, t)$ exists and the fluid velocity is given by its gradient. It is also assumed that the surface tensions on the free surface can be ignored and the water depth is finite. The velocity potential $\phi(x, y, z, t)$ satisfies the Laplace equation inside the fluid domain Ω

$$\nabla^2\phi(x, y, z, t) = 0 \quad \text{in } \Omega \tag{1}$$

On the instantaneous free surface, both the fully nonlinear kinematic and dynamic boundary conditions can be derived from the material derivatives and Bernoulli equation. The resulting

DOI: 10.1002/fld

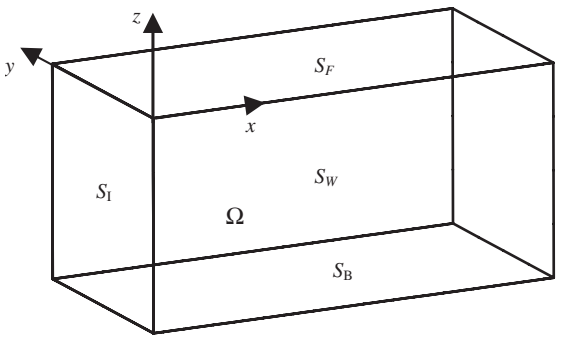

Figure 1. Coordinate systems and boundary surface.

equations on the free surface S_F can be deduced as the following:

$$\frac{\partial \eta}{\partial t} = -\frac{\partial \phi}{\partial x}\frac{\partial \eta}{\partial x} - \frac{\partial \phi}{\partial y}\frac{\partial \eta}{\partial y} + \frac{\partial \phi}{\partial z} \quad \text{on } S_F \tag{2}$$

and

$$\frac{\partial \phi}{\partial t} = -\frac{1}{2}\nabla\phi \cdot \nabla\phi - g\eta \quad \text{on } S_F \tag{3}$$

where η denotes the wave elevation on the instantaneous free surface profile and g is the gravitational acceleration. The corresponding linear kinematic and dynamic free surface conditions are given by

$$\frac{\partial \eta}{\partial t} = \frac{\partial \phi}{\partial z} \quad \text{on } z = 0 \tag{4}$$

and

$$\frac{\partial \phi}{\partial t} = -g\eta \quad \text{on } z = 0 \tag{5}$$

At the lateral walls S_W and bottom S_B of the tank, the impermeable condition is imposed.

At the inflow boundary S_I, a theoretical particle velocity profile along the vertical input boundary is used in this paper. The exact velocity profile of a true nonlinear wave under the given condition is not known *a priori*. Therefore, the best thing to do is to input the most reasonable waves along the input boundary. While linear or second-order Stokes regular/irregular waves are prescribed, the following velocity expression is used

$$v = v^{(1)} + v^{(2)} \tag{6}$$

where $v^{(1)}$ is the linear velocity and $v^{(2)}$ is the second-order velocity.

Here, for regular waves

$$v^{(1)} = n_x \frac{gAk}{\omega} \frac{\operatorname{ch} k(z+h)}{\operatorname{ch} kh} \cos(kx - \omega t) \tag{7}$$

DOI: 10.1002/fld

and

$$v^{(2)} = n_x \frac{3A^2\omega}{8}(2k)\frac{\mathrm{ch}\,2k(z+h)}{\mathrm{sh}^4\,kh}\cos 2(kx-\omega t) \tag{8}$$

where A, ω, k and h are wave amplitude, frequency, wave number and water depth, respectively.

For irregular waves, the velocity can be decomposed into N components with different frequencies [13]. Thus, the first order velocity can be written as

$$v^{(1)} = n_x \sum_{i=1}^{N} \frac{gA_ik_i}{\omega_i}\frac{\mathrm{ch}\,k_i(z+h)}{\mathrm{ch}\,k_ih}\cos(k_ix-\omega_it+\varepsilon_i) \tag{9}$$

and the second-order velocity as the following:

$$\begin{aligned} v^{(2)} = n_x \sum_{i=1}^{N}\sum_{j>i} \Bigg\{ & (k_i+k_j)A_iA_j\frac{G^+(\omega_i,\omega_j)}{D^+(\omega_i,\omega_j)}\frac{\mathrm{ch}(k_i+k_j)(z+h)}{\mathrm{ch}(k_i+k_j)h} \\ & \times\cos[(k_i+k_j)x-(\omega_i+\omega_j)t+(\varepsilon_i+\varepsilon_j)] \\ & +(k_i-k_j)A_iA_j\frac{G^-(\omega_i,\omega_j)}{D^-(\omega_i,\omega_j)}\frac{\mathrm{ch}(k_i-k_j)(z+h)}{\mathrm{ch}(k_i-k_j)h} \\ & \times\cos[(k_i-k_j)x-(\omega_i-\omega_j)t+(\varepsilon_i-\varepsilon_j)]\Bigg\} \\ & +n_x\sum_{i=1}^{\infty}k_iA_i^2\frac{G^+(\omega_i,\omega_i)}{D^+(\omega_i,\omega_i)}\frac{\mathrm{ch}\,2k_i(z+h)}{\mathrm{ch}\,2k_ih}\cos 2(k_ix-\omega_it+\varepsilon_i) \end{aligned} \tag{10}$$

where ε_i is the phase angel of each component wave and

$$D^{\pm}(\omega_i,\omega_j) = g(k_i\pm k_j)\,\mathrm{th}(k_i\pm k_j)h-(\omega_i\pm\omega_j)^2$$

$$G^{\pm}(\omega_i,\omega_j) = -g^2\left[\frac{k_ik_j}{\omega_i\omega_j}(\omega_i\pm\omega_j)(1\mp\mathrm{th}\,k_ih\cdot\mathrm{th}\,k_jh)+\left(\frac{k_i^2}{2\omega_i\,\mathrm{ch}^2\,k_ih}\pm\frac{k_j^2}{2\omega_j\,\mathrm{ch}^2\,k_jh}\right)\right]$$

From Equation (10), it can be seen that both sum and difference frequency components appear in the interaction terms at second-order for irregular waves.

Since the proposed problem is solved in the time domain, the initial water surface condition must be imposed as well. The initial calm water surface condition is applied in the present research. Thus, the initial velocity potential and wave elevation are

$$\phi = \eta = 0, \quad t\leqslant 0 \tag{11}$$

The direct boundary integral equation is derived to solve the prescribed boundary value problem by using the second Green's theorem. As far as the boundary integral equation is concerned, it is very important to choose a proper Green function, which will directly affect the size of the computational domain and calculation cost. If a simple Green function is used, all the boundary surfaces have to be contained in the computational domain [14, 15]. If the seabed is flat, a Green

DOI: 10.1002/fld

function including an image on the bottom can be used so that bottom surface is excluded in the computational domain [16, 17]. If the computational domain is symmetry on the centre line and the seabed is flat, a Green function including four images on the bottom and a lateral surface can be used so that only half the computational domain is considered [11, 18]. In this paper, a novel Green function satisfying the impermeable condition on the seabed and the two lateral walls is applied so that only the incident boundary and the free boundary are included in the computational domain. Then the Fredholm integral equation of the second kind can be derived as follows:

$$\alpha(p)\phi(p) - \int_{S_I} \phi(q)\frac{\partial G(p,q)}{\partial n}\,\mathrm{dS} + \int_{S_f} G(p,q)\frac{\partial \phi(q)}{\partial n}\,\mathrm{d}S$$
$$= -\int_{S_I} G(p,q)\frac{\partial \phi(q)}{\partial n}\,\mathrm{d}S + \int_{S_f} \phi(q)\frac{\partial G(p,q)}{\partial n}\,\mathrm{d}S \tag{12}$$

where $p=(x_0, y_0, z_0)$ and $q=(x, y, z)$ are source and field points, and $\alpha(p)$ is the solid angle. The Green function can be obtained by the superposition of the image of the Rankine source about the seabed and the infinite images about the two lateral walls. To ensure the convergence of the Green function, a factor $1/nB$ is subtracted from each term [19]. The Green function can be written as

$$G(p,q) = -\frac{1}{4\pi}[G_C(x-x_0, y-y_0, z-z_0) + G_C(x-x_0, y+y_0, z-z_0)$$
$$+ G_C(x-x_0, y-y_0, z+z_0+2h) + G_C(x-x_0, y+y_0, z+z_0+2h)] \tag{13}$$

where

$$G_C(X,Y,Z) = \frac{1}{\sqrt{X^2+Y^2+Z^2}}$$
$$+\sum_{n=1}^{\infty}\left(\frac{1}{\sqrt{X^2+(Y+2nB)^2+Z^2}} + \frac{1}{\sqrt{X^2+(Y-2nB)^2+Z^2}} - \frac{1}{nB}\right)$$

where B is the tank width, and h is water depth. A similar technique has ever been used to solve wave diffraction/radiation problems in frequency domain [20].

The potential ϕ on S_F in the right hand side of Equation (12) is assumed to be known from the time integration of the free surface conditions (3) and (5).

2.2. *Higher-order boundary element method*

The first step to solve the integral equation is to discretize the boundary surface with a number of elements. The geometry of each element is represented by shape functions, and thus the entire curved boundary can be approximated by a number of higher-order elements. Within the boundary elements, physical variables are also interpolated by the shape functions. Thus, the resulting

DOI: 10.1002/fld

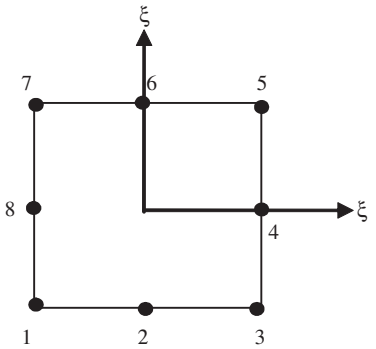

Figure 2. Quadrilateral elements of quadratic order.

approximations are written as

$$[x, y, z] = \sum_{k=1}^{K} h^k(\xi, \varsigma)[x_k, y_k, z_k] \tag{14}$$

$$\phi(\xi, \varsigma) = \sum_{k=1}^{K} h^k(\xi, \varsigma)\phi_k \tag{15}$$

$$\frac{\partial \phi}{\partial n} = \sum_{k=1}^{K} h^k(\xi, \varsigma)\left(\frac{\partial \phi}{\partial n}\right)_k \tag{16}$$

where (ξ, ς) represent the local intrinsic coordinates, $[x_k, y_k, z_k]$, ϕ^k, $(\partial\phi/\partial n)_k$ and h^k are the coordinates, potential, normal derivative of the potential and the shape function at the kth node, respectively; K is the number of nodes in the element (six for triangle and eight for quadrilateral in the present model).

Typical shape functions of 8-node quadrilateral elements shown in Figure 2 are written as

$$\begin{aligned} h^j(\xi, \varsigma) &= \tfrac{1}{4}\xi_j\xi(1 + \xi_j\xi)\varsigma_j\varsigma(1 + \varsigma_j\varsigma), \quad j = 1, 3, 5, 7 \\ h^j(\xi, \varsigma) &= \tfrac{1}{2}(1 - \xi^2)\varsigma_j\varsigma(1 + \varsigma_j\varsigma), \quad j = 2, 6 \\ h^j(\xi, \varsigma) &= \tfrac{1}{2}\xi_j\xi(1 + \xi_j\xi)(1 - \varsigma^2), \quad j = 4, 8 \end{aligned} \tag{17}$$

By substituting Equations (14)–(17) into Equation (12), the integral equation is formulated in the following form:

$$\alpha(p)\phi(p) - \sum_{i=1}^{Ne_2}\int_{-1}^{1}\int_{-1}^{1}\sum_{k=1}^{K} h^k(\xi, \varsigma)\phi_k \frac{\partial G(p, q(\xi, \varsigma))}{\partial n}|J(\xi, \varsigma)|\,\mathrm{d}\xi\,\mathrm{d}\varsigma$$
$$+ \sum_{i=1}^{Ne_1}\int_{-1}^{1}\int_{-1}^{1}\sum_{k=1}^{K} h^k(\xi, \varsigma)G(p, q(\xi, \varsigma))\frac{\partial \phi_k}{\partial n}|J(\xi, \varsigma)|\,\mathrm{d}\xi\,\mathrm{d}\varsigma$$

DOI: 10.1002/fld

$$= -\sum_{i=1}^{Ne_2}\int_{-1}^{1}\int_{-1}^{1} G(p, q(\xi,\varsigma))\frac{\partial\phi(q(\xi,\varsigma))}{\partial n}|J(\xi,\varsigma)|\,\mathrm{d}\xi\,\mathrm{d}\varsigma$$

$$+\sum_{i=1}^{Ne_1}\int_{-1}^{1}\int_{-1}^{1}\frac{\partial G(p, q(\xi,\varsigma))}{\partial n}\phi(q(\xi,\varsigma))|J(\xi,\varsigma)|\,\mathrm{d}\xi\,\mathrm{d}\varsigma \tag{18}$$

where $J(\xi,\eta)$ represents the Jacobian matrix relating the global coordinate and the local intrinsic coordinates in the ith element. Ne_1 and Ne_2 are the numbers of the discretized elements on the free surface and the incident surface, respectively.

The final system of equations is obtained by assuming that the discretized equations are satisfied exactly at a defined set of collocation points

$$Ax = b \tag{19}$$

where x is a vector of unknown potential and normal velocity; A is the influence matrix and b is the vector obtained from the integration of the single-layer and double-layer integrals in terms of the prescribed potential and velocity.

Since the discretized integral equation is always variant in time, all the boundary surfaces are regridded at every time step. The influence coefficients are also computed using the updated grids and known values. If the normal velocity on a boundary surface is known, the fluid velocity on the surface can be computed using the following equation:

$$\begin{bmatrix}\dfrac{\partial\phi}{\partial x}\\[2ex]\dfrac{\partial\phi}{\partial y}\\[2ex]\dfrac{\partial\phi}{\partial z}\end{bmatrix} = \begin{bmatrix}\dfrac{\partial x}{\partial\xi} & \dfrac{\partial y}{\partial\xi} & \dfrac{\partial z}{\partial\xi}\\[2ex]\dfrac{\partial x}{\partial\varsigma} & \dfrac{\partial y}{\partial\varsigma} & \dfrac{\partial z}{\partial\varsigma}\\[2ex] n_x & n_y & n_z\end{bmatrix}^{-1}\begin{bmatrix}\dfrac{\partial\phi}{\partial\xi}\\[2ex]\dfrac{\partial\phi}{\partial\varsigma}\\[2ex]\dfrac{\partial\phi}{\partial n}\end{bmatrix} \tag{20}$$

The first order derivative of wave elevation are also evaluated as

$$\begin{bmatrix}\dfrac{\partial\eta}{\partial x}\\[2ex]\dfrac{\partial\eta}{\partial y}\end{bmatrix} = \begin{bmatrix}\dfrac{\partial x}{\partial\xi} & \dfrac{\partial y}{\partial\xi}\\[2ex]\dfrac{\partial x}{\partial\varsigma} & \dfrac{\partial y}{\partial\varsigma}\end{bmatrix}^{-1}\begin{bmatrix}\dfrac{\partial\eta}{\partial\xi}\\[2ex]\dfrac{\partial\eta}{\partial\varsigma}\end{bmatrix} \tag{21}$$

where n_x, n_y, n_z are components of the unit normal vector in the x, y and z directions. The derivatives of geometric variables and potential with respect to the local coordinates can be represented by

$$\frac{\partial x}{\partial\xi} = \sum_k \frac{\partial h^k}{\partial\xi}x_k, \quad \frac{\partial\phi}{\partial\xi} = \sum_k \frac{\partial h^k}{\partial\xi}\phi_k, \ldots \tag{22}$$

2.3. Time marching for fully nonlinear free surface conditions

To update the fully nonlinear kinematic and dynamic free surface conditions at each time step, the 4th-order Runge–Kutta integration scheme and the semi-mixed Eulerian–Lagrangian approach are

DOI: 10.1002/fld

adopted. In the present calculation, the material-node approach is used, in which the free surface node is allowed to move in the vertical direction with nodal velocity ($\vec{v}$). The free surface node then should be updated at every time step. When the free-surface node is moving with velocity ($\vec{v}$), and the fully nonlinear free-surface conditions can be modified as follows in the semi-Lagrangian frame:

$$\frac{\delta\eta}{\delta t} = -\frac{\partial\phi}{\partial x}\frac{\partial\eta}{\partial x} - \frac{\partial\phi}{\partial y}\frac{\partial\eta}{\partial y} + \frac{\partial\phi}{\partial z} \quad \text{on } S_F \tag{23}$$

and

$$\frac{\delta\phi}{\delta t} = -\tfrac{1}{2}\nabla\phi\cdot\nabla\phi - g\eta + \frac{\delta\eta}{\delta t}\cdot\frac{\delta\phi}{\delta z} \quad \text{on } S_F \tag{24}$$

where the time derivative

$$\frac{\delta}{\delta t} = \frac{\partial}{\partial t} + \vec{v}\cdot\nabla \tag{25}$$

and velocity vector $\vec{v} = (0, 0, \delta\eta/\delta t)$

2.4. Ramp function

When the simulation is started, a ramp-function at the input boundary is applied. The ramp function prevents the impulse-like behaviour of the wavemaker and reduces the corresponding unnecessary transient waves. It makes the simulation more stable and steady state is reached earlier. In this paper, a ramp function is applied to the first two waves. The ramp function is given by [21]

$$f(t) = \begin{cases} 1, & t > 2T \\ \dfrac{1}{2}\left[1 - \cos\left(\dfrac{\pi t}{2T}\right)\right], & t \leqslant 2T \end{cases} \tag{26}$$

where T is the wave period.

2.5. Artificial damping beach

Toward the end of the computational domain, an artificial damping beach is applied on the free surface so that the wave energy is gradually dissipated in the direction of wave propagation. The profile and magnitude of the artificial damping have to be designed to minimize possible wave reflection at the entrance of the damping zone, while maximizing wave energy dissipation. In this paper, both φ- and η-type damping terms are added to the fully nonlinear dynamic and kinematic free-surface conditions as follows:

$$\frac{\delta\eta}{\delta t} = -\frac{\partial\phi}{\partial x}\frac{\partial\eta}{\partial x} - \frac{\partial\phi}{\partial y}\frac{\partial\eta}{\partial y} + \frac{\partial\phi}{\partial z} - \mu(x)\eta \quad \text{on } S_F \tag{27}$$

and

$$\frac{\delta\phi}{\delta t} = -\frac{1}{2}\nabla\phi\cdot\nabla\phi - g\eta + \frac{\delta\eta}{\delta t}\cdot\frac{\delta\phi}{\delta z} - \mu(x)\phi \quad \text{on } S_F \tag{28}$$

DOI: 10.1002/fld

In order to minimize the entrance reflection, the damping is designed to grow gradually to the target constant value in the following equation:

$$\mu(x) = \begin{cases} \omega \left(\dfrac{x - x_{\mathrm{b}}}{L_{\mathrm{b}}} \right)^2, & x > x_{\mathrm{b}} \\ 0 & \text{otherwise} \end{cases} \tag{29}$$

where x is the coordinate measured from the inflow boundary, x_{b} is the distance from the inflow boundary to the beach and L_{b} is the beach length. In the following sections, L_{b} will be chosen as different values according to different problems.

2.6. Time step and stability

The present numerical experiments indicate that a maximum time step of $T/40$ can be used before numerical instability occurs. Thus, the time step $T/40$ is employed in the following numerical examples. Another type of instability, i.e. the so-called saw-tooth instability, is treated by a numerical smoothing technique covering five neighbouring points. It is applied to the wave elevation and potential every 10 time steps.

3. NUMERICAL RESULTS AND DISCUSSIONS

For illustration, several numerical simulations are carried out for linear and fully nonlinear, regular and irregular waves in the proposed numerical wave tank using analytical input waves at the inflow boundary.

3.1. Simulation of linear waves

3.1.1. Linear regular wave. At first, the present numerical scheme is verified by simulating linear regular waves. For this simulation, the linear boundary value problem is solved at each time step. The wavelength and period are $\lambda = 5.15$ m and $T = 2.1$ s, respectively. The wave slope is chosen as $kA = 0.033$. The principal dimensions of the wave tank are L(length) $\times$ B(width) $\times$ h(depth)=15.45 $\times$ 0.3 $\times$ 0.8 m, in which a damping layer with a length of one wavelength is arranged on the free surface towards the end of tank to absorb the outputting waves. The mesh density distributed along the wave tank is 10 elements per wavelength. The simulated linear regular wave elevation at the location $(0.28L, 0.5B)$ is presented in Figure 3 and compared with the theoretical input waves, where the wave elevation is normalized by the amplitude of incident waves. The numerical results are in good agreement with the theory except the leading transient waves. Near the end of the damping zone, the wave profile at a location $(0.9L, 0.5B)$ is shown in Figure 4. It can be seen that the wave height is sufficiently reduced by viscous dissipation. The above results show that the present modelling scheme works well with the given problem.

3.1.2. Linear irregular waves. We next consider a linear irregular progressing wave as input at the inflow boundary. Linear irregular waves are obtained by linear superposition of four waves of periods $T = 1.20$, 1.13, 0.93 and 0.85 s, phase angles $\varepsilon = 0$, $\pi/8$, $\pi/4$ and $\pi/2$, respectively. Assuming the wave slope $kA = 0.1$ for each wave, the corresponding wave numbers and amplitudes can thus be obtained. The principal dimensions of the wave tank are $L \times B \times h = 4.43 \times 0.4 \times 0.8$ m.

DOI: 10.1002/fld

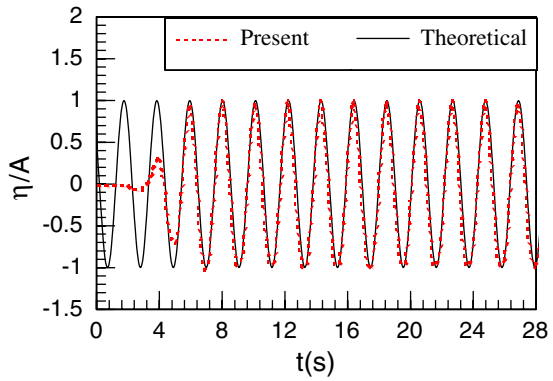

Figure 3. Comparison of simulated linear results with the linear theoretical solutions.

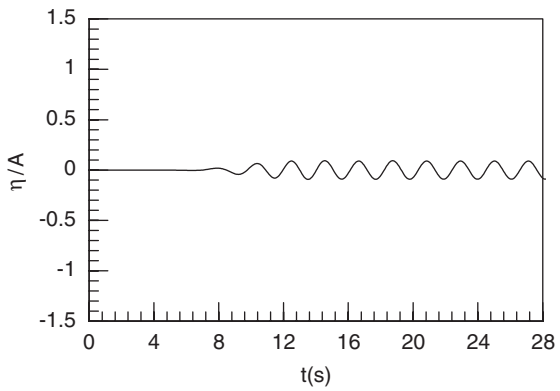

Figure 4. Wave elevation at a location in damping zone.

In order to dissipate the waves as much as possible, the length of the damping layer is taken as the maximum wavelength of the four waves on the free surface towards the end of tank. The mesh density distributed along the tank is 10 elements per minimum wavelength. Time histories of wave elevations at two different locations a $(0.5L, 0.5B)$ and b $(1.0L, 0.5B)$ along the symmetric line of the wave tank are shown in Figure 5 respectively, where the wave elevation is normalized by the sum of amplitudes of the incident wave components. From Figure 5(a), it can be seen that the simulated results agree fairly well with the linear theoretical ones [13], which imply that the present numerical scheme is effective even for irregular waves. From Figure 5(b), it can be seen that great wave energy has been successfully dissipated when the output wave reaches the end of wave tank, which shows the present damping layer also works well for irregular waves.

3.2. Simulation of nonlinear waves

In this section, several fully nonlinear, regular and irregular waves are simulated while the second-order analytical nonlinear waves are considered as the inputs at the inflow boundary.

DOI: 10.1002/fld

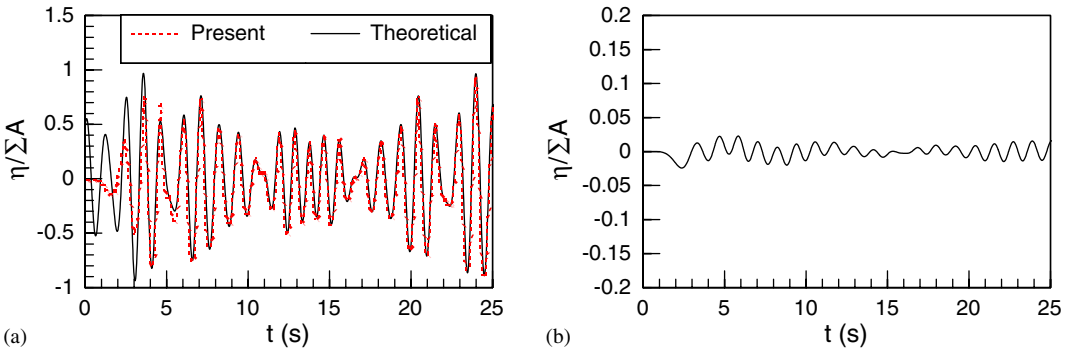

Figure 5. Time histories of linear irregular wave elevations at two locations: (a) $(0.5L, 0.5B)$; and (b) $(1.0L, 0.5B)$.

3.2.1. Regular second-order Stokes waves. The second-order Stokes waves are prescribed on the inflow boundary at every time step, and the resulting waves are simulated by enforcing the fully nonlinear free surface condition. The wave length and frequency are $\lambda = 5.16\,\text{m}$ and $\omega = 3.0$, respectively. The wave slope is chosen as $kA = 0.1$. Dimensions of the wave tank are $L \times B \times h = 18.07 \times 0.6 \times 0.8\,\text{m}$. At the end of the tank, the damping layer is applied for a distance of 1.5 times wave length. The mesh density distributed along the wave tank is 15 elements per wavelength.

The simulated fully nonlinear regular wave elevations at two locations a $(0.32L, 0.5B)$ and b $(0.57L, 0.5B)$ are presented in Figure 6 and compared with the second-order theoretical input waves. The numerical results are in good agreement with the second-order theoretical solutions except for the leading transient waves. It shows that the wave amplitude remains almost unchanged after the initial development of the waves and the nonlinear wave features are also exhibited apparently, such as higher crests and smaller troughs. The perspective view of the simulated wave at $t = 10T$ is illustrated in Figure 7. From the figure, we can see that the reflection from the radiation boundary does not seem to exist besides for steady wave propagation.

3.2.2. Irregular Stokes waves with two wave components. A Stokes wave formed by the second-order interaction of two waves is used as input at the inflow boundary at every time step. The periods of the two waves are 1.20 and 1.40 s, phase angles are 0 and $\pi/2$, respectively. Wave slope is defined as $kA = 0.05$ for each wave. The principal dimensions of the wave tank are $L \times B \times h = 7.28\,\text{m} \times 0.32\,\text{m} \times 0.8\,\text{m}$. The mesh density distributed along the tank is 15 elements in a smaller wavelength. The simulated nonlinear wave elevation is compared with the second-order irregular Stokes theoretical solution [13] at the position $(0.50L, 0.50B)$ in Figure 8. Figure 9 provides a comparison of computed fully nonlinear irregular wave profile and the second-order irregular Stokes theoretical one along the central line of the tank at time $t = 10.8\,\text{s}$. Reasonable agreements are evident between numerical and analytical solutions in Figures 8 and 9, except in the damping zone. Figure 10 shows the perspective view of the fully nonlinear irregular wave elevation at time $t = 14.4\,\text{s}$. There are no apparent reflection phenomena existing at the end of the wave tank.

DOI: 10.1002/fld

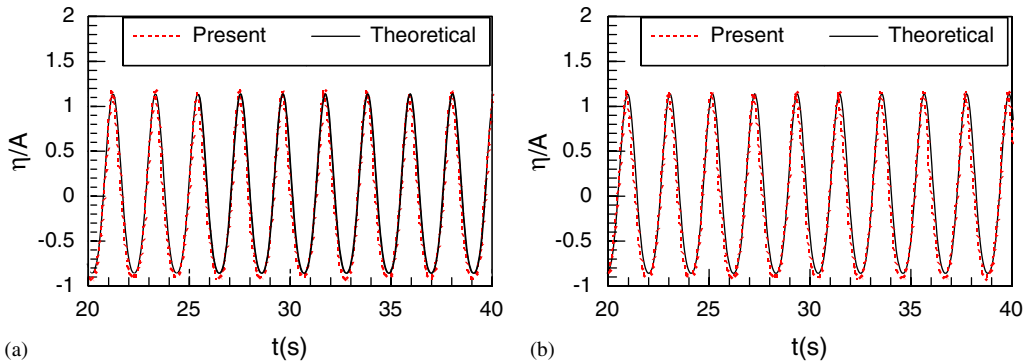

Figure 6. Comparison of simulated fully nonlinear regular waves with the second-order theoretical solutions at two different locations: (a) $(0.32\,L,\ 0.5\,B)$; and (b) $(0.57\,L,\ 0.5\,B)$.

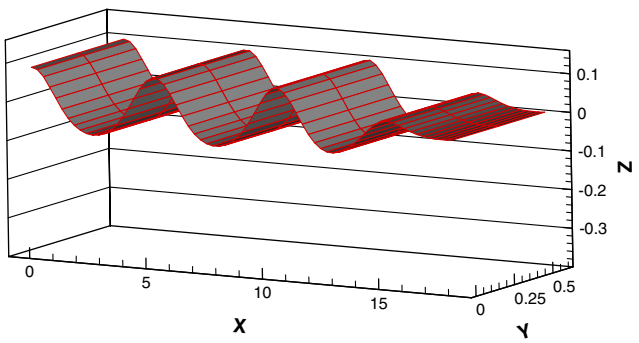

Figure 7. Perspective view of fully nonlinear regular wave elevation at $t = 10T$.

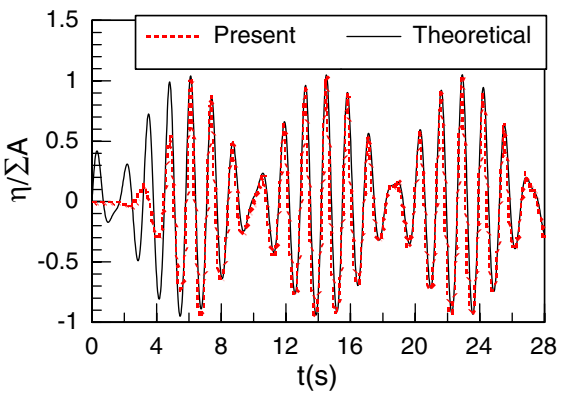

Figure 8. Comparison of simulated results with the second-order Stokes irregular waves at a location.

DOI: 10.1002/fld

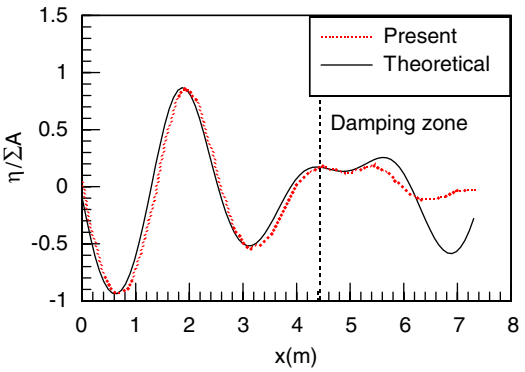

Figure 9. Comparison of the fully nonlinear irregular wave profiles at $t = 10.8$ s.

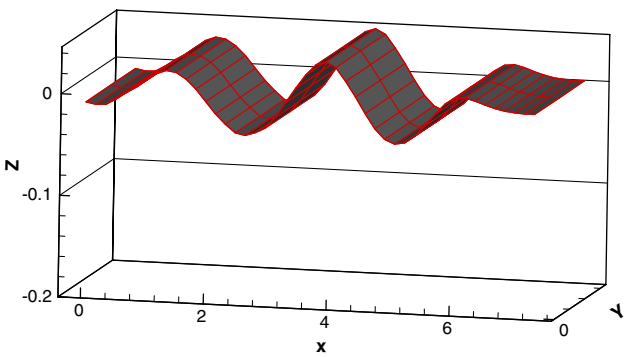

Figure 10. Perspective view of nonlinear irregular wave profile at time $t = 14.4$ s.

3.2.3. Irregular Stokes waves with four wave components. The superposition of four second-order waves is fed at the inflow boundary, whose periods and phase angles are the same as the above linear case. The wave slope is chosen as $kA = 0.05$ for each wave. Dimensions of the wave tank are $L \times B \times h = 5.56 \times 0.2 \times 0.78$ m. The wave elevations at two different locations a $(0.04L, 0.5B)$ and b $(0.44L, 0.5B)$ are compared with the second-order irregular Stokes theoretical solutions [13] in Figure 11. The simulated wave elevations agree fairly well with the theoretical ones, which imply that the present numerical scheme is effective even for more irregular waves. Figure 12 shows the comparison of two wave profiles along the central line of wave tank at two different times $t = 11.16$ and 17.21 s. There are no apparent reflection phenomena existing at the end of the wave tank. Figure 13 shows the perspective view of fully nonlinear irregular wave elevations at $t = 9.3$ and 15.81 s.

DOI: 10.1002/fld

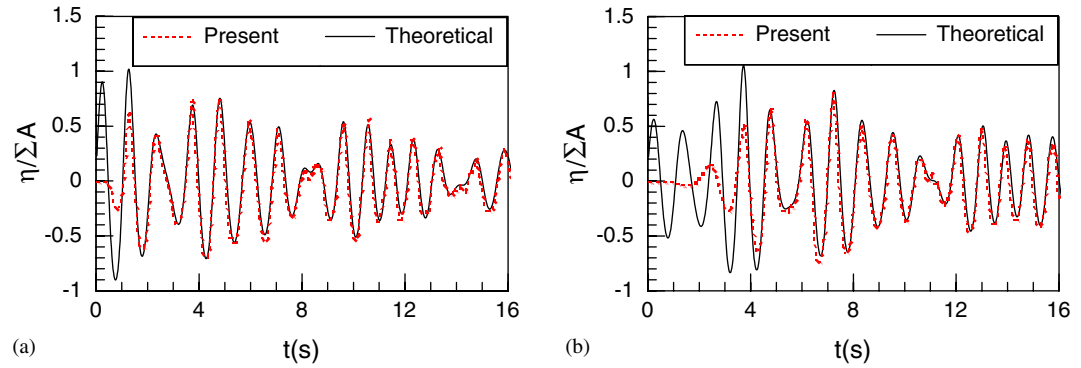

Figure 11. Comparison of simulated fully nonlinear irregular waves with the second-order irregular Stokes theoretical solutions at two different positions: (a) $(0.04L, 0.5B)$; and (b) $(0.44L, 0.5B)$.

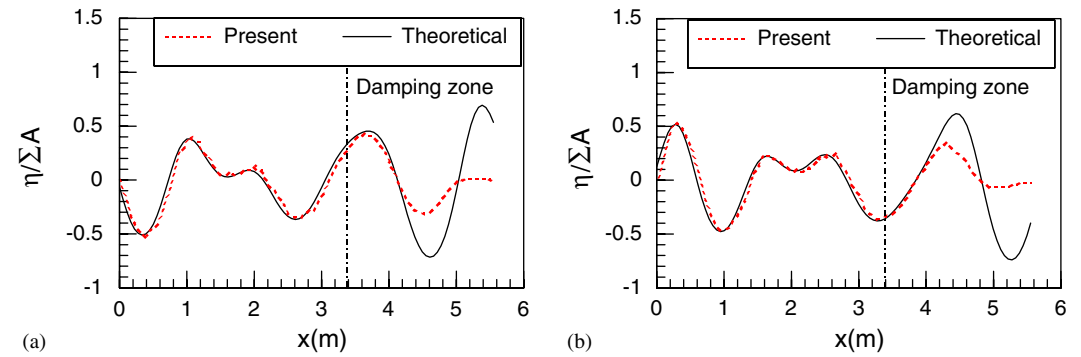

Figure 12. Comparison of two wave profiles along the central line of the tank at two different times: (a) $t = 11.16$ s; and (b) $t = 17.21$ s.

4. CONCLUSIONS

In the present work, a time-domain numerical scheme is implemented to simulate linear and fully nonlinear, regular and irregular waves by a simple source HOBEM. A new Green function is applied in the whole fluid domain so as to exclude the lateral boundaries and bottom boundary. The linear and fully nonlinear boundary value problems are solved separately and thus the boundary conditions are imposed accordingly. The boundary integral equation formulated by a quadratic-order boundary element method is solved in the time-stepping procedure. The instantaneous wave elevations and potentials on the free surface are updated using the fourth-order Runge–Kutta method. The open boundary is modelled by using an absorbing beach. In the case of nonlinear simulation, the second order irregular Stokes waves with two/four wave components are used as the incident waves being fed through the inflow boundary. The linear and fully nonlinear irregular wave simulations are verified by comparing the computed results with theoretical values. Excellent agreement is achieved between the predictions and analytical solutions. The proposed numerical

DOI: 10.1002/fld

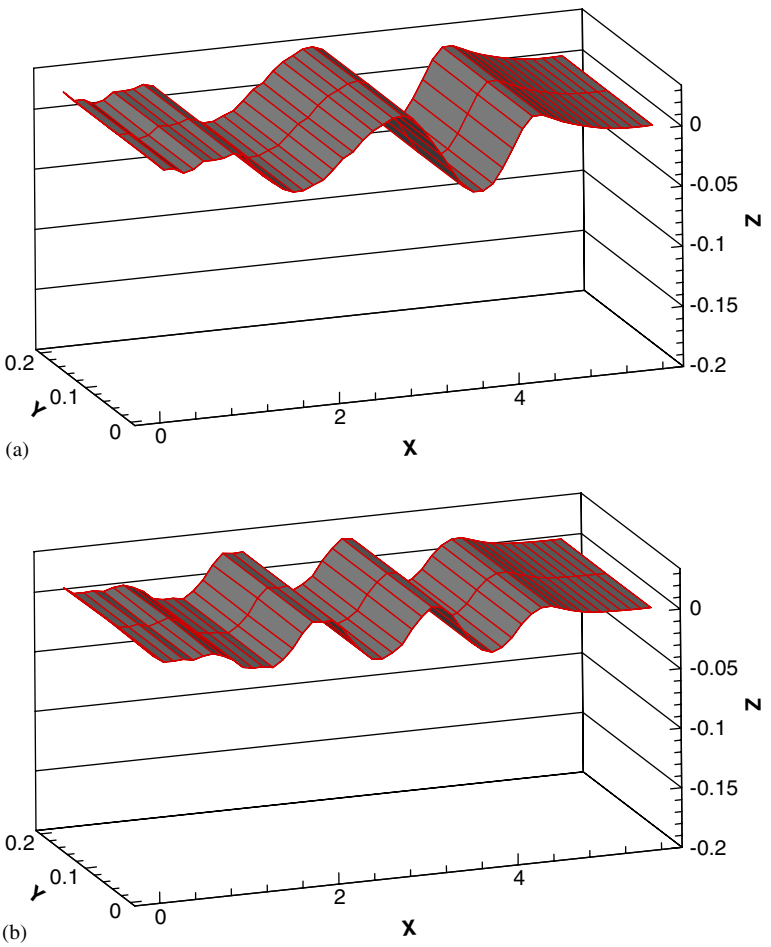

Figure 13. Perspective view of the fully nonlinear irregular wave elevation at two times: (a) $t = 9.3$ s; and (b) $t = 15.81$ s.

scheme can be easily extended to fully nonlinear irregular wave–body interaction problems, but the high computational overheads need to be overcome. Further study will be done to simulate fully nonlinear irregular wave–body interaction problems by a more efficient HOBEM accelerated by the fast multipole expansion technique, whose efficiency in calculation speed and computer storage has already been verified [22].

ACKNOWLEDGEMENTS

The authors gratefully acknowledge the financial support provided by the Program for Changjiang Scholars and Innovative Research Team in University (Grant No. IRT0420) and Research Fund for the Doctoral Program of Higher Education (Grant No. 20030141006).

DOI: 10.1002/fld

REFERENCES

1. Xu H. Numerical study of fully nonlinear water waves in three dimensions. *Sc.D. Dissertation*, Department of Ocean Engineering, MIT, Cambridge, 1992.
2. Romate JE. The numerical simulation of nonlinear gravity waves in three dimensions using higher-order panel method. *Ph.D. Dissertation*, University of Twente, Enschede, The Netherlands, 1989.
3. Kim DJ, Kim MH. Wave–current–body interaction by a time-domain high-order boundary element method. *Proceedings of Seventh International Offshore and Polar Engineering Conference*, vol. 3, Honolulu, ISOPE, 1997; 107–115.
4. Celebi MS. Nonlinear transient wave-body interactions in steady uniform currents. *Computer Methods in Applied Mechanics and Engineering* 2001; **190**:5149–5172.
5. Scorpio SM, Bech RF, Korsmeyer FT. Nonlinear water wave computations using a multipole accelerated desingularized method. *Proceedings of 21st International Symposium on Naval Hydrodynamics*, Tronheim, 1996.
6. Beck RF. Time-domain computations for floating bodies. *Applied Ocean Research* 1994; **16**:267–282.
7. Wu GX, Ma QW, Eatock Taylor R. Numerical simulation of sloshing waves in a 3D tank based on a finite element method. *Applied Ocean Research* 1998; **20**:337–355.
8. Hu P, Wu GX, Ma QW. Numerical simulation of nonlinear wave radiation by a moving vertical cylinder. *Ocean Engineering* 2002; **29**(14):1733–1750.
9. Wang CZ, Khoo BC. Finite element analysis of two-dimensional nonlinear sloshing problems in random excitations. *Ocean Engineering* 2005; **32**:107–133.
10. Xu Q, Pawlowski JS, Baddour RE. Simulation of nonlinear irregular waves by Green–Naghdi theory. *Workshop on Water Waves and Floating Bodies*, Newfoundland, Canada, 1993.
11. Boo SY. Linear and nonlinear irregular waves and forces in a numerical wave tank. *Ocean Engineering* 2002; **29**:475–493.
12. Tanizawa K. The state of the art on numerical wave tank. *Proceedings of Fourth Osaka Colloquium on Seakeeping Performance of Ships*, Osaka, 2000.
13. Schäffer HA. Second-order wavemaker theory for irregular waves. *Ocean Engineering* 1996; **21**(1):47–88.
14. Grilli ST, Guyenne P, Dias F. A fully nonlinear model for three-dimensional overturning waves over arbitrary bottom. *International Journal for Numerical Methods in Fluids* 2001; **35**:829–867.
15. Sung HG, Grilli ST. Numerical modeling of nonlinear surfaces waves caused by surface effect ships dynamics and kinematics. *Proceedings of Fifth International Offshore and Polar Engineering Conference*, Seoul, Korea, 2005.
16. Fructus D, Clamond D, Grue J, Kristiansen Ø. An efficient model for three-dimensional surface wave simulations. Part I: Free space problems. *Journal of Computational Physics* 2005; **205**:665–685.
17. Clamond D, Fructus D, Grue J, Kristiansen Ø. An efficient model for three-dimensional surface wave simulations. Part II: Generation and absorption. *Journal of Computational Physics* 2005; **205**:686–705.
18. Skourup J, Cheung KF, Bingham HB. Loads on a 3D body due to second-order wave and a current. *Ocean Engineering* 2000; **27**:707–727.
19. Newman JN. Approximation of free-surface Green function. In *Wave Asymptotics*, Martin PA, Whickham GR (eds). Cambridge University Press: Cambridge, MA, 1992; 107–142.
20. Teng B, Eatock Taylor R. New higher-order boundary element methods for wave diffraction/radiation. *Applied Ocean Research* 1995; **17**:71–77.
21. Baudic SF, Williams AN, Kareem A. A two-dimensional numerical wave flume—Part 1: Nonlinear wave generation, propagation and absorption. *Journal of Offshore Mechanics and Arctic Engineering*, *Transaction of the ASME* 2001; **123**:70–75.
22. Teng B, Ning DZ. Application of a fast multipole BIEM for flow diffraction from a 3D body. *China Ocean Engineering* 2004; **18**(2):291–298.

DOI: 10.1002/fld